

PAPER • OPEN ACCESS

# Carbon-assisted chemical vapor deposition of hexagonal boron nitride

To cite this article: Ariel Ismach *et al* 2017 *2D Mater.* **4** 025117

## Manuscript version: Accepted Manuscript

Accepted Manuscript is “the version of the article accepted for publication including all changes made as a result of the peer review process, and which may also include the addition to the article by IOP Publishing of a header, an article ID, a cover sheet and/or an ‘Accepted Manuscript’ watermark, but excluding any other editing, typesetting or other changes made by IOP Publishing and/or its licensors”

This Accepted Manuscript is© .



Original content from this work may be used under the terms of the [Creative Commons Attribution 3.0 licence](https://creativecommons.org/licenses/by/3.0/). Any further distribution of this work must maintain attribution to the author(s) and the title of the work, journal citation and DOI.

View the [article online](#) for updates and enhancements.

# Carbon-Assisted Chemical Vapor Deposition of Hexagonal Boron Nitride

Ariel Ismach,<sup>1,2</sup> Harry Chou,<sup>1</sup> Patrick Mende,<sup>3</sup> Andrei Dolocan,<sup>4</sup> Rafik Addou,<sup>5</sup> Shaul Aloni,<sup>6</sup> Robert Wallace,<sup>5</sup> Randall Feenstra,<sup>3</sup> Rodney S. Ruoff,<sup>1,7,8,9</sup> and Luigi Colombo<sup>10</sup>

<sup>1</sup>Department of Mechanical Engineering and the Materials Science and Engineering Program, the University of Texas at Austin, Austin, TX 78712.

<sup>2</sup>Department of Materials Science and Engineering, Tel Aviv University, Ramat Aviv, Tel Aviv 6997801, Israel.

<sup>3</sup>Department of Physics, Carnegie Mellon University, Pittsburgh, Pennsylvania 15213.

<sup>4</sup>Texas Materials Institute, the University of Texas at Austin, Austin, TX 78712.

<sup>5</sup>Department of Materials Science and Engineering, the University of Texas at Dallas, Dallas, Texas 75080, United States.

<sup>6</sup>The Molecular Foundry, Lawrence Berkeley National Laboratory, Berkeley, California 94720, United States.

<sup>7</sup>Center for Multidimensional Carbon Materials, Institute of Basic Sciences Center, Ulsan National Institute of Science and Technology, Ulsan, 44919, Republic of Korea.

<sup>8</sup>Department of Chemistry, Ulsan National Institute of Science and Technology (UNIST), Ulsan 44919, Republic of Korea.

<sup>9</sup>School of Materials Science and Engineering, Ulsan National Institute of Science and Technology (UNIST), Ulsan 44919, Republic of Korea.

<sup>10</sup>Texas Instruments, 13121 TI Boulevard, Dallas, Texas 75243, United States.

*Hexagonal boron nitride, chemical vapor deposition, carbothermal reduction, surface oxidation, ToF-SIMS, LEEM.*

---

**ABSTRACT:** We show that in a low-pressure chemical vapor deposition (CVD) system, the residual oxygen and/or air play a crucial role in the mechanism of the growth of hexagonal boron nitride (*h*-BN) films on Ni foil ‘enclosures’. *Hexagonal*-BN films grow on the Ni foil surface via the formation of an intermediate boric-oxide (BO<sub>x</sub>) phase followed by a thermal reduction of the BO<sub>x</sub> by a carbon source (either amorphous carbon powder or methane), leading to the formation of single- and bi-layer *h*-BN. Low energy electron microscopy (LEEM) and diffraction (LEED) were used to map the number of layers over large areas; Raman spectroscopy, time-of-flight secondary ion mass spectroscopy (ToF-SIMS), x-ray photoelectron spectroscopy (XPS) and scanning tunneling microscopy (STM) were used to characterize the structure and physical quality of the ultra-thin *h*-BN film. The growth procedure reported here leads to a better understanding and control of the synthesis of ultra-thin *h*-BN films.

---

## INTRODUCTION

Major advances have been made over the last decade or so in the growth of large area polycrystalline and single crystal graphene.<sup>1-3</sup> The transport properties of the grown graphene layers have been preserved by the use of hexagonal boron nitride as the substrate and a top dielectric for top-gated field effect transistors, which is not like when other dielectrics are used as substrates or gate dielectrics. Today, the quality of CVD graphene is equivalent to or exceeds that of exfoliated graphene from natural graphite.<sup>4</sup> Hexagonal-BN has the same physical structure and lattice parameter as graphene but also, and perhaps more importantly, it is flatter, stiffer, and free from dangling bonds compared with other substrates such as SiO<sub>2</sub>.<sup>5</sup> In addition, *h*-BN possesses other important properties such as high thermal conductivity<sup>6</sup> and a direct wide band-gap among others making it useful for many other applications such as deep ultra-violet (DUV) lasing.<sup>7</sup> To date, a large number of papers describing the growth of large area *h*-BN have been reported, but controlled growth (number of layers) of high quality *h*-BN, in terms of flatness and point defects is still challenging. We present new data on the basic mechanisms of single layer and bi-layer *h*-BN growth by chemical vapor deposition (CVD) that will help the future development of large area high quality *h*-BN films.

The basic understanding of single crystal and bilayer graphene film growth has been gained in part from growing these films in copper ‘enclosures’.<sup>8</sup> The use of a copper enclosure has enabled the growth of graphene with the same quality as the best-exfoliated graphene from natural graphite.<sup>4,9-11</sup> Specifically, growth studies of graphene inside copper enclosures (pockets) have led to ultra-large single crystal and single-layer graphene crystals as well as to important insights into the effect of oxygen on the growth process.<sup>3,8</sup> However, at this time we do not have an equivalent understanding of the growth mechanism of *h*-BN on any substrate. Single, few-layer, and multilayer *h*-BN has been grown on polycrystalline metal films and foils, and the formation of few layer *h*-BN on Ni,<sup>12-15</sup> Co,<sup>13,14,16</sup> Fe,<sup>17</sup> Pt<sup>18,19</sup> and Cu<sup>20,21</sup> has been reported, but with limited control and understanding of the growth process. Monolayer growth of *h*-BN on Cu has been reported at a low partial pressure of the BN precursor (ammonia-borane).<sup>22</sup> Muller *et al* demonstrated three step *h*-BN epitaxial-growth on Rh (111):<sup>23</sup> (i) a boration, (ii) oxidation step and (iii) nitration. However, in order to achieve full coverage in ultra-high vacuum (UHV) conditions, these three steps had to be repeated several times. In yet another paper, Behura *et al*<sup>24</sup> proposed the formation of *h*-BN films on silica initiated by a boron-oxygen bond. Other successful approaches include the use of graphene as a template, followed by its conversion to *h*-BN<sup>25-27</sup> and the epitaxial growth of high quality few-layer *h*-BN on sapphire at high temperatures (~1400°C).<sup>28</sup>

Here we report the carbothermal formation of ultra-thin *h*-BN films on the interior surface of a nickel foil enclosure. We show that, on the interior surface of the nickel enclosure, the growth of *h*-BN is aided by the formation of an intermediate phase, boron oxide (BO<sub>x</sub>), followed by the reduction of the BO<sub>x</sub> by carbon to form an ultra-thin *h*-BN layer. The BO<sub>x</sub> layer prevents diffusion of B and N into the Ni<sup>13,14</sup> and thus, inhibit the formation of multi-layer *h*-BN by a precipitation process, typical to its growth on Ni.<sup>16</sup> The resulting *h*-BN films formed using our new process contain 1 or 2 layers, as measured by LEEM and LEED. Carbothermal formation of BN<sup>29-32</sup> and BN nanotubes<sup>33</sup> has already been reported, however, to our knowledge, this is the first time this technique is used to grow single- and bi-layer *h*-BN with large crystal sizes. Our results suggest that the growth of *h*-BN can be tailored by controlling the chemistry of the Ni surface when exposed to borazane.

## RESULTS AND DISCUSSION

Hexagonal-BN growth on Ni surfaces has been reported by various groups,<sup>12,14-16,34</sup> with most showing multi-layer-film growth. In the case of *h*-BN growth on polycrystalline Ni and Co the growth has been reported to be a process of diffusion of B-N or B and N species thorough the metal followed by segregation (during cooling due to supersaturation) to form the *h*-BN phase.<sup>13-16,35</sup>

In this work, substrates such as flat Ni foils and Ni foil enclosures were used to grow *h*-BN by CVD using borazane as the precursor. The growth of *h*-BN on flat Ni foils, the exterior of Ni enclosures led to similar results, *i.e.* few-layer to thick *h*-BN films, as reported

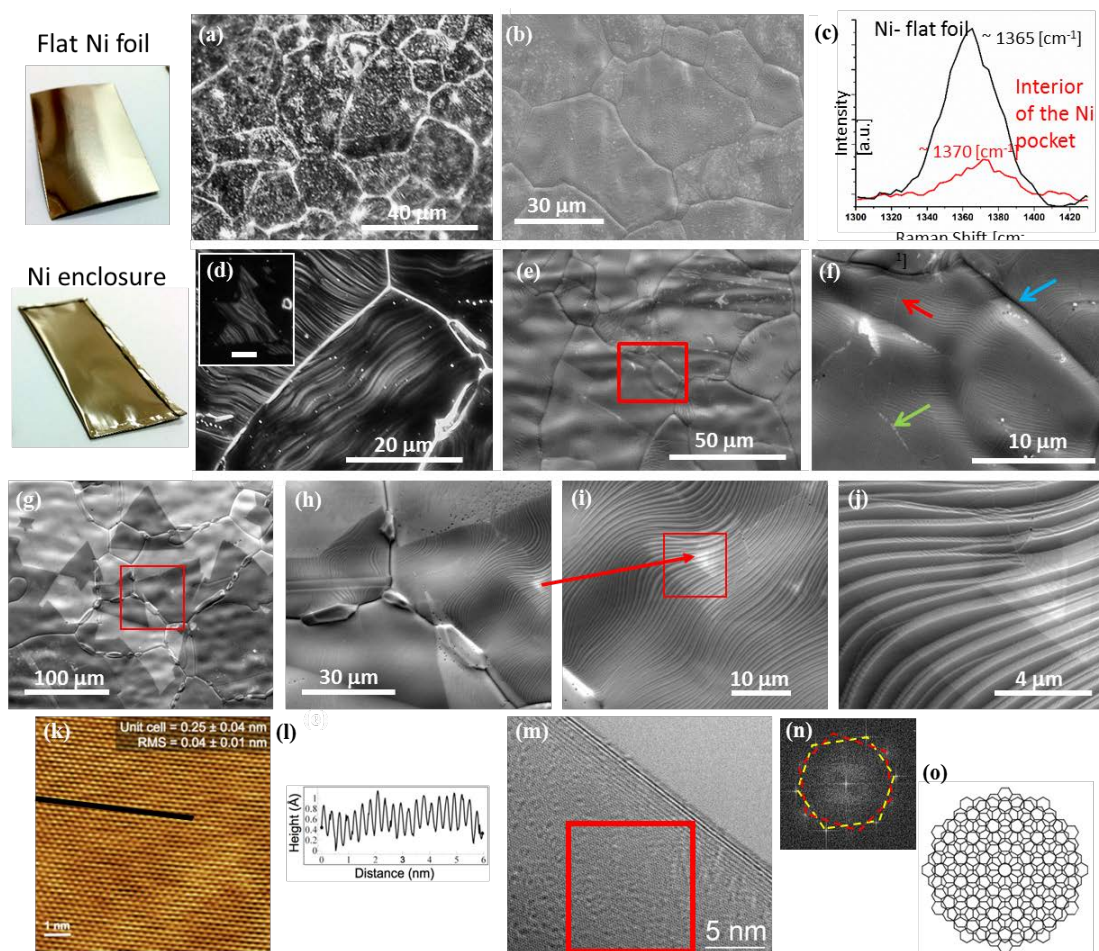


Figure 1: Synthesis of thick and ultra-thin *h*-BN films. (a) DF-OM and (b) SEM images of thick *h*-BN films on a Ni foil substrate. (c) Raman spectrum of thick (black) and thin (red) *h*-BN films. (d) DF-OM and (e)-(f) SEM images of ultra-thin *h*-BN films on the interior surface of a Ni enclosure. The scale bar in the inset of (d) is 20  $\mu\text{m}$ . In (f): the blue arrow points to a Ni grain boundary, the red arrow to a wrinkle in the *h*-BN film and the green to a crack or incompletely grown *h*-BN. Figures (g)-(j) show SEM images with increasing magnification of ultra-large single-crystal domains ( $\sim 100$  microns) and triangular ad-layers. (k) high-resolution STM imaging showing the hexagonal lattice in an ultra-thin *h*-BN film and its atomic smoothness along the black line (l). (m) Cross-sectional HR TEM image showing a bi-layer and its Moiré pattern. (n) FFT image of the red-square area in (m) showing two-hexagonal patterns rotated by a  $\sim 40^\circ$ . (o) Shows a schematic of the moiré-pattern created by two hexagonal lattices rotated by  $30^\circ$ .

previously.<sup>15</sup> In the case of Ni enclosures, however, no *h*-BN was detected on the *interior surface*, in contrast to the case of graphene growth in similar Cu enclosures.<sup>3,8</sup> However, when a small amount of carbon was added, either amorphous carbon powder in the interior of the enclosure or a low flow of methane gas, ultra-thin *h*-BN domains or continuous films were obtained inside the enclosure, depending on growth conditions. The carbon addition had no effect on the *h*-BN growth on flat surfaces or the exterior of the enclosure. Figure 1 shows a comparison between the growth of continuous *h*-BN films on (a-c) flat Ni substrates and (d-f) enclosures (with  $\sim 1\text{mg}$  of amorphous carbon in its interior) as seen by optical microscopy (OM), scanning electron microscopy (SEM) images, and Raman spectroscopy. Ultra-thin *h*-BN layers were observed on the inside surface of the Ni enclosure through contrast of the few layers on the nickel surface nanofacets (in dark-field OM (DF-OM) or SEM).<sup>36</sup> When a thick layer of *h*-BN is grown, no steps are detected, (Figure 1 a). In the case of a bare Ni substrate (no growth), nanofacets are usually not observed, most likely because the Ni surface is “damaged” as a result of oxidation. These results suggest that an ultra-thin layer of *h*-BN protects the Ni facet structures<sup>36</sup> (Figure 1 d), which appear as a series of intact curved steps. In the SEM image of the *h*-BN obtained on the interior surface of the enclosure (Figure 1 f), wrinkles (red arrow), uncovered Ni areas (green

arrow) and a Ni grain boundary (light blue arrow) are clearly seen. A series of SEM images of *h*-BN on the inside of the Ni enclosure are also shown in Figures 1 (g)-(j), where large single crystal triangular domains (around 100 microns) and their ad-layers are clearly visible. High-resolution scanning tunneling microscopy (STM) image, Figure 1 (k), and a line profile (along the black line in k), (l), demonstrates the atomic flatness of the film. The hexagonal lattice can be easily observed in the STM image whereas (k) shows the plan view TEM (m) image. In the latter, a bi-layer is shown with a Moiré pattern caused by a  $\sim 30^\circ$  rotation between the *h*-BN layers as shown in the FFT image, (n), calculated for the red square area in (m). A schematic representation of a  $30^\circ$  rotation between the layers is depicted in (o).

In addition to the results described above, the use of amorphous carbon powder in the interior of the enclosure had its drawbacks as well. First, the powder was mostly dissolved into the Ni at the growth temperature, and segregated to form a graphitic film in the area that was in mechanical contact with the carbon powder (Figure S5) upon cooling. The rest of the interior of the enclosure was covered with a continuous *h*-BN film or isolated triangular domains, depending on growth conditions and these areas were graphitic phase-free. Second, the controllability of the process was rather weak and the achievement of a continuous ultra-thin *h*-BN layer not observed because of the non-uniformity of the a-C in the enclosure. Hence, alternative carbon sources were considered.

Having seen that carbon can assist the growth of ultra-thin *h*-BN layers in the interior of the Ni enclosures, we evaluated the use of another carbon source, methane (flow rate of 2-5 sccm) using the same experimental conditions. The resulting *h*-BN films were similar to the case where a-C was used, thick layers on flat Ni substrates and ultrathin ones in the interior of the enclosure. However, there was one important and significant difference when using  $\text{CH}_4$ , the *h*-BN inside the enclosure fully covered the Ni surface versus partial surface coverage in the presence of a-C, as shown in Figure 2. Figure 2(a) shows a schematic of the growth process, and Figures 2(b-e) show the growth results for two growth times while the Ni was exposed to ammonia borane and methane: 2 min, (b - c) and 5 min, (d - e). For short exposure times, single polygonal domains are observed; however, for exposures longer than 5 minutes, a continuous ultra-thin layer was obtained.

Characterization of single and few layer *h*-BN by Raman spectroscopy over large areas (mapping) has been difficult due to the low intensity of the *h*-BN signal, in contrast to graphene. Because of this shortcoming, other methods need to be used to detect and map the number of layers of *h*-BN films. In order to determine the thickness and crystallinity of our *h*-BN films we used low-energy electron microscopy (LEEM). This method has been extensively used to determine the number of layers for both graphene<sup>37-39</sup> and *h*-BN,<sup>34,40</sup> by examining the low-energy electron reflectivity (LEER) spectra. Here, we used LEEM to map *h*-BN thickness over the Ni surface, as shown in Figure 3. A typical LEEM image is shown in (a) with (b) showing a map of the number of layers (blue-1 layer, red-2 layers), extracted from the LEER spectra displayed in (c). LEER spectra are recorded at every pixel within the image of (a), and (c) displays some of these spectra. In such

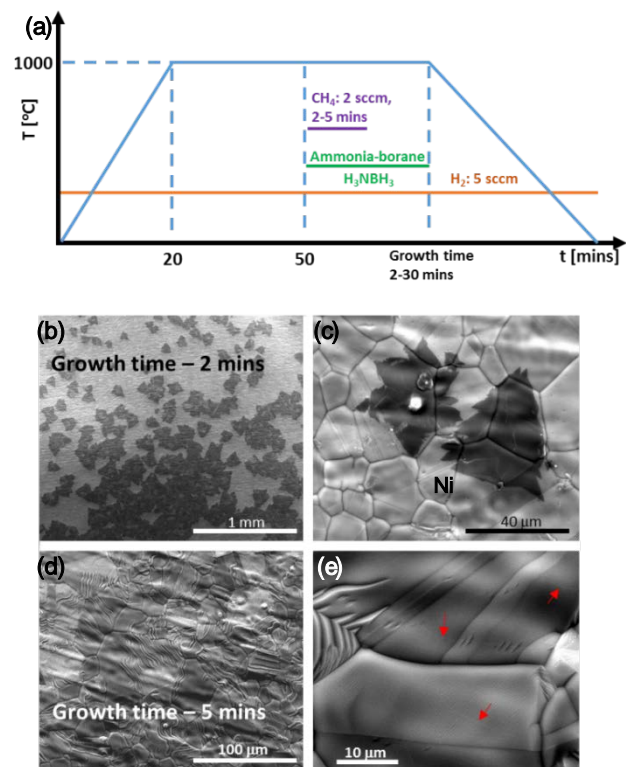


Figure 2: Synthesis of large ultra-thin *h*-BN films by a methane-assisted approach. (a) growth conditions used in this experiments. AB stands for ammonia borane. (b)-(c) SEM images of isolated and large domains after 2-minute growth. (d)-(e) continuous ultra-thin films after 5-minute growth.



spectra, reflectivity *minima* occur at energies of specific electronic states of the system; the spectra thus provide a “fingerprint” of the atomic arrangements on the surface.<sup>34</sup> Considering first the spectra at locations C and D, these are characterized by distinct reflectivity minima at about 3 eV and at 8 - 9 eV. The 3 eV minimum arises from an *interlayer* electronic state that occurs *between* two layers of *h*-BN, whereas the 8-9 eV minimum is associated with electronic states that occur *on* the *h*-BN planes (as opposed to between the planes).<sup>34</sup> Thus, these two spectra definitely establish the presence of two *h*-BN layers on the surface at these locations. Moving to the spectrum at location B, the higher energy minimum near 8 eV is still present, but the lower energy one at 3 eV is absent. Thus, this type of spectrum definitively establishes the presence of only a single *h*-BN layer.<sup>34</sup> Finally, for the spectrum at location A, we now see some features reminiscent of spectrum B, but at the same time the intensity of the reflectivity above 8 eV is significantly reduced. This type of curve is not typical of the ones that we generally obtain for these surfaces, and its interpretation is not completely clear. It appears that there is little, if any *h*-BN in this region of the surface, and indeed, spectrum A is somewhat similar to those that we have observed on bare metal surfaces.<sup>38</sup> Tentatively, we assign the location A and surrounding area to 0 ML of *h*-BN. By analyzing the spectra from each point in (a), the map shown in (b) was obtained.<sup>41</sup> Several samples and areas were tested using this method and the results were consistent, *i.e.* large-areas were covered with 1 and 2 layers of *h*-BN.

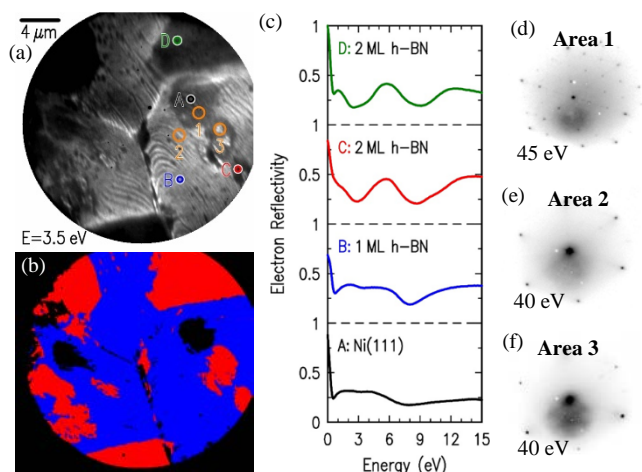


Figure 3: LEEM and  $\mu$ LEED characterization. (a) LEEM image of *h*-BN/Ni. (b) LEEM map of *h*-BN thickness, showing the presence of one and two *h*-BN layers as determined from the spectra in (c) at each point over the film surface in the field of view. Blue and red denote single-layer and double-layer *h*-BN, respectively. (c) A series of reflectivity spectra from different points in (a), from A to D. In C and D, two reflectivity minima are observed near 3 and at 8 - 9 eV, indicative of 2 ML *h*-BN. In B, only a single minimum near 8 eV is found, indicative of 1 ML *h*-BN. For spectrum A, no distinct minima are observed, and tentatively the spectrum is assigned to little or no *h*-BN on the surface. (d)-(f)  $\mu$ LEED images from area 1, 2 and 3 in (a). Area 1 is bare Ni (111); it is apparent that the diffraction points of the *h*-BN from areas 2 and 3 overlap with those of the Ni (111).

Figures 3(d)-(f) show selected-area LEED ( $\mu$ LEED) patterns, obtained from the areas indicated in (a). Based on the LEER spectra, area 1 contains little if any *h*-BN, area 2 contains 1 ML of *h*-BN, and area 3 contains 2 ML of *h*-BN. The LEED patterns of areas 2 and 3 are seen to contain six primary spots in a hexagonal arrangement; these spots arise from the *h*-BN on the surface. For the pattern from area 1, six spots at the same locations of those of areas 2 and 3 can again be seen, but many additional spots are also seen. Based on the LEER spectrum indicating  $\ll 1$  ML *h*-BN coverage in this area, we assign this pattern to bare Ni, and from its hexagonal arrangement we deduce that the Ni surface has a (111) orientation. The fact that the six diffraction spots in areas 2 and 3 are aligned with those of area 1 indicates that the *h*-BN is aligned with the underlying nickel.<sup>34</sup> Figures S6 and S7 contain additional LEEM and  $\mu$ LEED data.

### Growth Mechanism

The *h*-BN growth was carried out in an ammonia-borane partial pressures of 10-100 mTorr where the pressure was controlled by heating the precursor to a specific temperature to control the evaporation rate. We found that in order to obtain *h*-BN on the *interior surface of the enclosure* (with carbon present), a minimum chamber ammonia-borane partial pressure of  $\sim 50$  mTorr was needed. Below this pressure no *h*-BN was observed. As mentioned above, the minimum pressure of the growth system is  $\sim 8$  mTorr. At this base pressure the oxygen partial pressure in the chamber is significant and needs to be taken in consideration as it can oxidize the surface of the Ni, potentially forming a uniform layer of  $\text{NiO}_x$  on the surface. The ammonia-borane is introduced into the chamber at

~50 mTorr partial pressure immediately after annealing the Ni in hydrogen as shown schematically Fig. 2a. The thermal decomposition of the ammonia-borane on the surface of NiO<sub>x</sub>/Ni is a complex process involving various thermal reduction and dehydrogenation steps,<sup>42</sup> leading eventually to the formation of *h*-BN. In the case of carbon-free growth, the B and N species reach the surface of the Ni (flat substrates and exterior of the enclosure) where the B-containing compounds are believed to react with the NiO<sub>x</sub> leading to the formation of B<sub>2</sub>O<sub>3</sub> as shown by the XPS spectra in Fig. 5. The formation of boron oxide was already observed in our previous report on flat substrates.<sup>15</sup> The rest of the B species react with the N species to form the *h*-BN film. However, inside an enclosure, we hypothesize, that the amount of precursor that diffuses through the small apertures in the mechanically folded enclosure is significantly lower, and the degree of Ni oxidation is most likely higher due to the trapped air, in comparison to the exterior surface. This is similar to the case of the CVD of graphene using Cu enclosures,<sup>3</sup> where it was shown that the oxidation of the surface decreased the density of nuclei which led to large area graphene single crystals.<sup>3</sup> Such a model is consistent with the kinetic theory of gases where a small gap in the enclosure (relative to the interior surface area) impacts the mass flow, and diffusion rate,<sup>13</sup> of the precursor and other vapor phase compounds into the enclosure. In order to shed light on potential intermediate reactions of the precursors with the oxidized Ni surface, free energy of formation calculations were performed. Figure 4 shows a summary of such calculations plotted as a function of temperature [see supporting information for calculation details]. Figure 4 (a) represents the free-energy of formation as a function of temperature for boron and nickel oxides. It can be seen that the B<sub>2</sub>O<sub>3</sub> phase is thermodynamically preferable over NiO as shown for various potential chemical reactions in the CVD process. Figure 4 (b) shows a similar plot but for the BN phase formation, comparing reactions with and without carbon. These calculations suggest that, in the presence of carbon, the free-energy of formation of the BN phase is more negative, *i.e.* thermodynamically more favorable. This supports our data that indicate the formation of ultra-thin *h*-BN layers in the presence of carbon. It should be noted that NH<sub>3</sub> in a similar way as CH<sub>4</sub> should also reduce the B<sub>2</sub>O<sub>3</sub> to form BN. In our experiments, however, the ammonia-assisted growth led only to the partial formation of multi-layer and non-homogeneous *h*-BN domains (Figure S1). Also important to note, from the Ellingham diagram, is that B<sub>2</sub>O<sub>3</sub> cannot be reduced by annealing in H<sub>2</sub> at the growth temperatures used in this work (Figure S10). Thus, the introduction of small amounts (~1 mg) of amorphous carbon into the enclosure or a few sccm (up to 5) of methane flow, while exposing the Ni surface to the ammonia-borane, leads to *h*-BN growth by a reduction of boron oxide by a carbo-thermal process.<sup>29,43,44</sup>

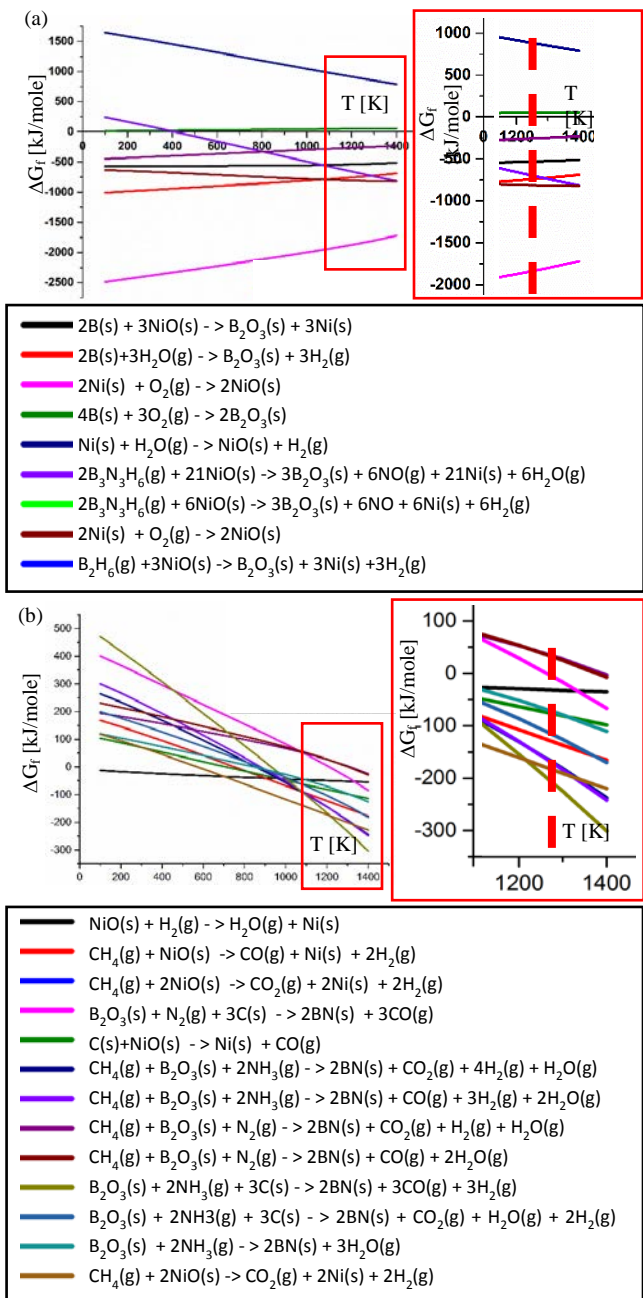


Figure 4: (a) Thermodynamic calculations for B and Ni oxidation and (b) for the formation of the BN phase. In both, the inset in red margins is an expansion of the larger graph around the growth temperature (~1273 K). The potential chemical reactions are shown below each graph.

1  
2  
3  
4  
5  
6  
7  
8  
9  
10  
11  
12  
13  
14  
15  
16  
17  
18  
19  
20  
21  
22  
23  
24  
25  
26  
27  
28  
29  
30  
31  
32  
33  
34  
35  
36  
37  
38  
39  
40  
41  
42  
43  
44  
45  
46  
47  
48  
49  
50  
51  
52  
53  
54  
55  
56  
57  
58  
59  
60

*Ex-situ* XPS and ToF-SIMS chemical characterization were also used to support our results and the growth mechanism. Figure 5 shows the SEM images and XPS spectra of four different samples (all four taken from the interior surface of the Ni enclosures). Figure 5 summarizes the data for 4 different experiments, each column contains the data of a different sample and every row contains the data acquired for the B1s, N1s, C1s and O1s core levels, from top to bottom. Comparing the B1s spectra of the different samples, it is evident that the B-O phase is present in all of the samples except for the CH<sub>4</sub>-assisted growth. It should be noted that in the carbon-free sample, the B1s peak is associated with the B-O binding energy ( $E_b = 192.4$  eV, which corresponds to the B<sub>2</sub>O<sub>3</sub>),<sup>45,46</sup> and correlates with the lack of *h*-BN on these samples. The contribution of the B-O phase to the B1s peak decreases with increasing *h*-BN quality and coverage. Similarly, the N1s peak intensity increases with the *h*-BN coverage (from top to bottom). We note that the amount of carbon present on the sample surface, as indicated by the C1s peak area, is reduced with the coverage of *h*-BN and the use of amorphous carbon or methane, Figure S11. This suggests that the carbon used to aid the B<sub>2</sub>O<sub>3</sub> reduction is not incorporated into the *h*-BN lattice. This conclusion is supported by the absence of a graphitic signal in the Raman spectra, Figures S2, S3 and S4. In addition, a reduction of the oxygen content is observed with increasing coverage and quality of the *h*-BN layer (Figure S11). Analysis of the relative amounts of carbon and oxygen are shown in Figure S11, calculated from the respective peak areas.

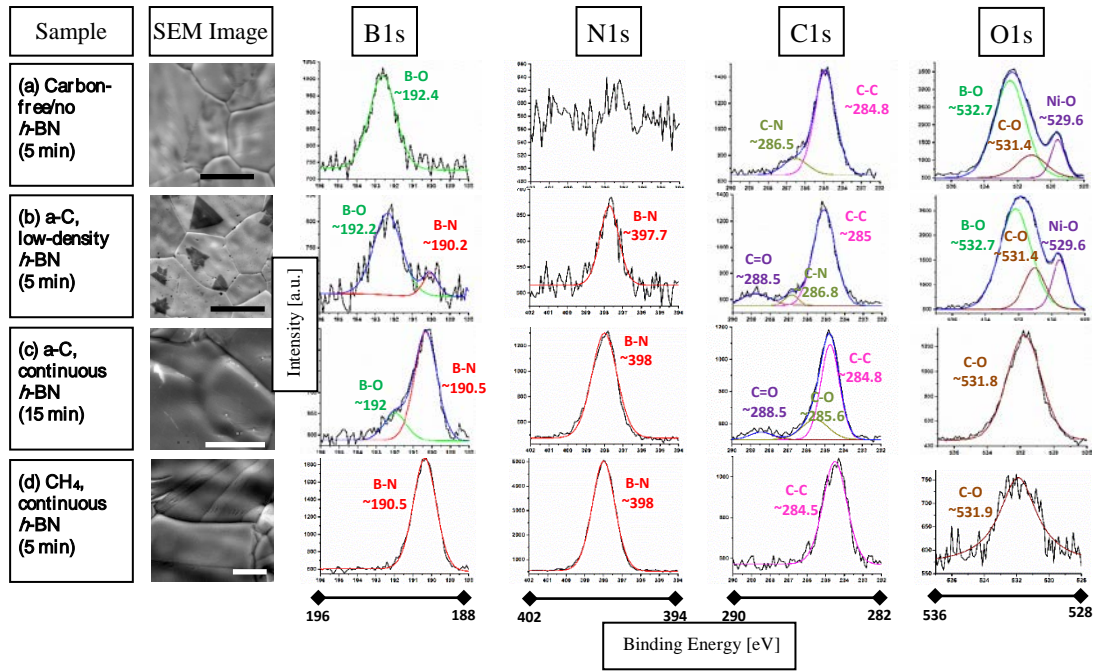


Figure 5. XPS Characterization. Every row shows the result for a different sample in which a representative SEM image of the interior of the enclosure is shown in (a)-(d): (a) Carbon-free (no *h*-BN- 10 min growth), (b) a-C (low density *h*-BN domain area- 5 min growth), (c) a-C (continuous *h*-BN film area – 15 min growth) and (d) CH<sub>4</sub>-assisted growth (continuous *h*-BN film- 5 min growth). Scale bars are 50  $\mu$ m for (a) and (b), 10  $\mu$ m in (c) and (d). The columns for the XPS spectra regions from left to right show the results for the B1s, N1s, C1s and O1s core levels. In all the cases, the x-axis shows the binding energies in eV and the y-axis, the intensity in arbitrary units. The Full scale in binding energy is underneath each column and the relevant peaks noted.

To corroborate the above results, we used ToF-SIMS, an ultra-high chemical and surface sensitive technique<sup>47,48</sup> which has a high lateral resolution (~200 nm) and enables chemical mapping. Figures 6 (a)-(c) show the chemical maps for BN<sup>-</sup>, BO<sub>2</sub><sup>-</sup> and NiO<sup>-</sup> ions



respectively after  $\sim 1$  second of  $\text{Cs}^+$  sputtering ( $\sim 0.1$  nm depth) to clean the surface of adsorbates. Hexagonal BN triangular domains are observed in Figure 6 (a), where the  $\text{BO}_2^-$  and  $\text{NiO}^-$  distributions are spatially separated from the  $h$ -BN covered areas. The ToF-SIMS data further support the growth mechanism, that is,  $\text{NiO}_x$  is reduced by B species to form  $\text{B}_2\text{O}_3$  which is further reduced by C (or  $\text{CH}_x$ ) and N species to form  $h$ -BN and thus leading to a lower concentration of  $\text{B}_2\text{O}_3$  and  $\text{NiO}_x$  species underneath the  $h$ -BN (brighter color indicates a higher concentration). Figures 6 (d)-(f) show the same elemental mapping but after sputtering for 4 seconds (at  $\sim 0.6$  nm depth), which completely removed the  $h$ -BN and the  $\text{B}_2\text{O}_3$  layer. The  $\text{NiO}_x$  on the other hand, seems to be thicker in the  $h$ -BN-free regions ( $\sim 2$  nm) and it took about 10 s to remove it, (Figure S12 and S13). The depth conversion<sup>48,49</sup> of the  $\text{Cs}^+$  sputtering time is shown in Figures 6 (g)-(h) and S12, where each data point represents 1 second of  $\text{Cs}^+$  sputtering. The ToF-SIMS analysis shows that  $\text{B}_2\text{O}_3$  is on the surface and is removed by 4 seconds of sputtering,  $<1$  nm thick. This appears to be crucial for the formation of ultra-thin  $h$ -BN (1 and 2 layers as shown by LEEM measurements), as it inhibits the diffusion of the B (and N) into the Ni, as demonstrated previously.<sup>12-15,35</sup> This suggests that the B-assisted reduction of  $\text{NiO}_x$  and the subsequent formation of  $\text{B}_2\text{O}_3$  fixes the B atoms at the surface of the metal until the  $h$ -BN is formed. Figures 6 (g) and (h) show profiles from  $h$ -BN and  $h$ -BN-free areas supporting this analysis. However, further experiments are needed to understand the reason and mechanism for the formation of a bi-layer, as detected in the LEEM results. As mentioned above, we also evaluated the effect of ammonia gas instead of carbon (amorphous or methane) as a possible  $\text{B}_2\text{O}_3$  reducing agent<sup>50</sup> to form  $h$ -BN and indeed it was detected inside the Ni enclosures despite the lack of carbon (Figure S1). However, the  $h$ -BN grown using  $\text{NH}_3$  was not continuous for the conditions that we used. Further experiments are needed to understand the differences between carbon- and ammonia-assisted  $h$ -BN growth, indeed there are competing reactions occurring in the system, each with complex rate coefficients.

We have demonstrated the synthesis of ultra-thin  $h$ -BN films composed of 1 and 2 layers with large-domains by carbo-thermal assisted-growth in the interior of a Ni enclosure. The  $h$ -BN films were characterized by LEEM and  $\mu\text{LEED}$ . The formation the mono- and

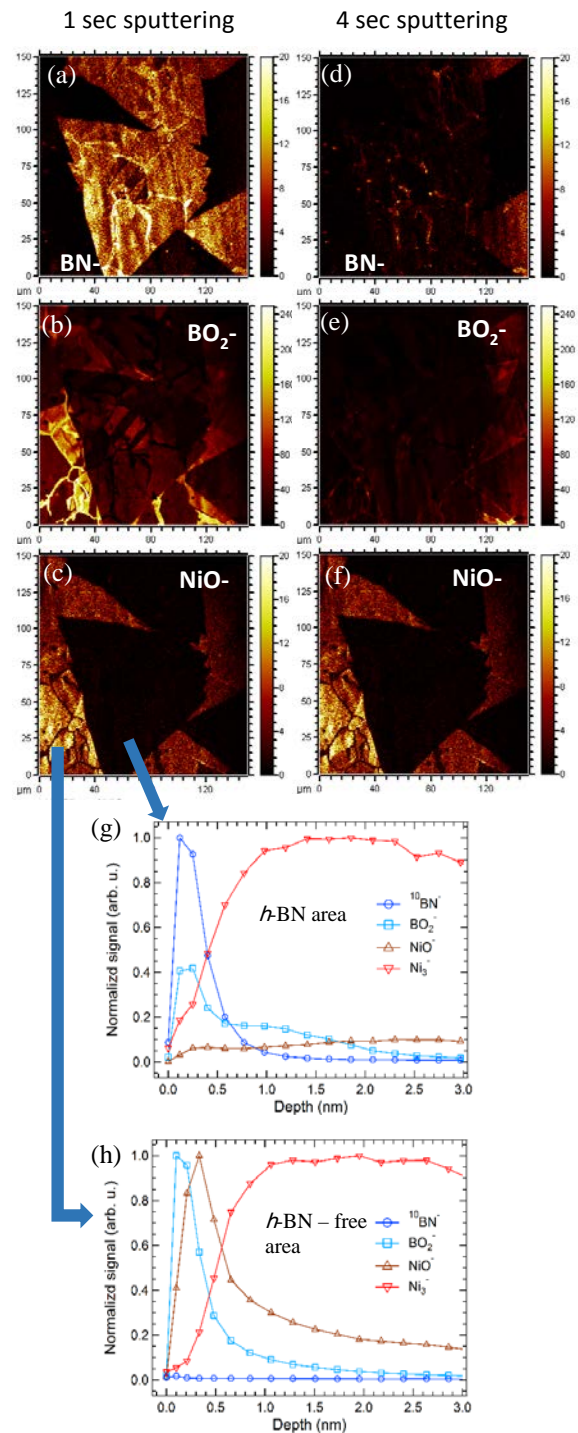


Figure 6: TOF-SIMS characterization. (a)-(c) Maps of the  $\text{BN}^-$ ,  $\text{BO}_2^-$  and  $\text{NiO}^-$  secondary ions, after 1 second of  $\text{Cs}^+$  sputtering ( $\sim 0.1$  nm depth) to clean the surface. (d)-(f) Same location maps of the same ions after 4 seconds of  $\text{Cs}^+$  sputtering ( $\sim 0.6$  nm depth), showing that the BN and boron oxide layers were sputtered away, (d) and (e) show that BN and boron oxide layers are completely removed, in contrast to the Ni oxide layer which needed about 10 seconds of  $\text{Cs}^+$  sputtering ( $\sim 2$  nm depth) to be completely removed (Figure S12). (g) and (h) show profiles of the relevant ions for  $h$ -BN and  $h$ -BN-free areas, respectively. Scan size in all the cases are  $150 \mu\text{m}^2$ .

bi-layer *h*-BN, in contrast to the growth of thick *h*-BN on Ni and Co foils,<sup>12,15</sup> is explained by an intermediate formation of boron oxide on the interior of the enclosures which inhibits the diffusion of B and N into the bulk of the metal. The boron oxide is then reduced using carbon in the form of amorphous carbon or CH<sub>4</sub> gas leaving the B to react with the NH<sub>3</sub> thus forming *h*-BN. *Ex-situ* XPS and ToF-SIMS were performed to identify boron oxide in *h*-BN free areas/samples. In the case of a fully covered Ni surface with *h*-BN, boron oxide was not observed.

The results presented in this paper emphasize the importance of having a basic understanding and control of the growth environment in *h*-BN growth by CVD. We also show that controlled layer growth of *h*-BN on Ni (or other metals) can be achieved by a suitable metal surface chemical modification. Further experiments and calculations are needed in order to fully understand the influence of the crystal orientation of the Ni on such a growth process. In principle, by carefully controlling the growth system ambient chemistry, the same results could be obtained on flat surfaces.

## EXPERIMENTAL

***h*-BN growth:** Three different types of samples were tested in this work: 1. flat Ni foils, 2. flat Ni thin films and 3. Ni foil enclosures. The incorporation of carbon to the system was achieved by adding ~1 mg of amorphous carbon (99% <sup>13</sup>C enriched amorphous carbon powder was used, Cambridge Isotope Laboratories, Inc. CLM-402-1) to the Ni enclosures or by flowing CH<sub>4</sub> (~1-5 sccm, 99.999 %, Airgas). The synthesis of *h*-BN was carried out by LPCVD as reported previously.<sup>15</sup> Briefly, the growth substrate was placed in the center of a 1 inch diameter quartz tube, which was placed in a tube furnace. The chamber was then evacuated to ~8 mTorr base pressure. Hydrogen (10 sccm, 99.999 %, Airgas) was then flowed through the system. The sample was heated to the growth temperature (typically 1000-1050°C) and the sample was annealed at such conditions for 30 mins. Thereafter, the hydrogen flow was reduced to 5 sccm and the ammonia-borane was independently heated to 80-100° C to produce the desired partial pressure of ammonia-borane; the partial pressure of ammonia-borane was monitored to be around 60 mTorr. The growth was performed for times ranging between 5 and 30 mins.

### Characterization:

Optical microscopy (OM): bright and dark field, Zeiss Axiovert 100A Light Microscope.

Scanning electron microscopy (SEM): FEI Quanta-600

Transmission electron microscopy (TEM): JEOL 2100-F 200 kV Field – with silicon nitride coated copper grids, Ted Pella, 215365.

Raman spectroscopy (RS): Witec Alpha 300 micro-Raman confocal microscope.

X-ray photoelectron spectroscopy (XPS): was conducted using a commercial X-ray photoelectron spectrometer (Kratos Axis Ultra), using a monochromated Al K $\alpha$  X-ray source ( $h\nu = 1486.7$  eV), electrostatic lens optics, and a multichannel plate and delay line detector coupled to a hemispherical analyzer (180° with a 165 mm mean radius). The photoelectron takeoff angle was normal to the surface of the sample and 45° with respect to the X-ray beam. High-resolution spectra were collected with a pass energy of 20 eV. The pressure in the analysis chamber was typically  $2 \times 10^{-9}$  Torr during data acquisition.

Scanning tunneling microscopy (STM): The sample was loaded into an ultra-high vacuum (UHV) surface analysis system with a base pressure in low  $1 \times 10^{-10}$  mbar range described elsewhere.<sup>51,52</sup> The *h*-BN surface was imaged using an Omicron variable temperature STM without any thermal treatment. The STM images were obtained at room temperature and in the constant-current mode, with an etched tungsten tip.

**Time-of-flight secondary ion mass spectroscopy (ToFSIMS):** The ToF-SIMS data were collected with a commercial ION-ToF SIMS 5 instrument which was configured in the high-resolution burst alignment (BA) mode that enabled mapping at ~200 nm lateral resolution. The samples were probed with a 30 keV Bi<sup>+</sup> analysis ion beam (18 ns burst pulse duration) and a 1 keV Cs<sup>+</sup> sputter beam (~55 nA sample current), which were raster scanned over areas of 150 x 150  $\mu\text{m}^2$  and 250 x 250  $\mu\text{m}^2$ , respectively. The Cs<sup>+</sup> sputtering rates were calculated at ~0.12 nm s<sup>-1</sup> and 0.22 nm s<sup>-1</sup> for *h*-BN and Ni, respectively. All spectra were collected in negative polarity with a mass resolution > 5000 ( $m/\delta m$ ) at a base pressure < 2 x 10<sup>-9</sup> Torr.

**Low-energy electron microscopy (LEEM):** We performed LEEM and selected-area  $\mu\text{LEED}$  in an Elmitec LEEM III. In this apparatus, incident and reflected/diffracted electrons are separated from one another by a 60° magnetic beam splitter. All LEEM images here were acquired in bright-field mode, wherein the electron-beam is momentum filtered such that only secularly reflected electrons participate in image formation. By obtaining many such images at different incident electron energies, we then extract LEER spectra from given points on the surface. These experimental spectra are then compared to a first-principles method for describing LEER which has been described elsewhere.<sup>37-39</sup>  $\mu\text{LEED}$  is performed by the introduction of a collimating aperture which restricts the size of the electron beam to ~ 1  $\mu\text{m}$  in diameter, allowing us to locally probe the crystallinity across the surface.

## ASSOCIATED CONTENT

**Supporting Information.** The supporting information includes additional LEEM and  $\mu\text{LEED}$  data, energy of formation calculations for the different oxide phases and the CH<sub>4</sub>-assisted growth results, TOF-SIMS mapping and depth profiling, Raman spectroscopy and mapping of *h*-BN ad-layers.

## AUTHOR INFORMATION

### Corresponding Author

\* [aismach@tauex.tau.ac.il](mailto:aismach@tauex.tau.ac.il)

### Author Contributions

The manuscript was written through contributions of all authors. / All authors have given approval to the final version of the manuscript.

## ACKNOWLEDGMENT

AI acknowledges support from the Israel Science Foundation, project number 1784/15. RSR was supported in part by the Institute for Basic Science (IBS-R019- D1). The work at The University of Texas at Austin (UTA) was supported by the Keck Foundation grant no. 749046 and the Department of Defense—Navy grant N00014-10- 1-0254. We also acknowledge the NSF grant DMR-0923096 used to purchase the TOF-SIMS instrument at Texas Materials Institute, UTA. Material synthesis and characterization was also supported by the South West Academy of Nanoelectronics (SWAN 2.0, grant 2013-NE-2400) and the Center for Low Energy Systems Technology (LEAST), one of the six centers supported by the STARnet phase of the Focus Center Research Program, a Semiconductor Research Corporation program sponsored by MARCO and DARPA.

## REFERENCES

- (1) Li, X.; Cai, W.; Colombo, L.; Ruoff, R. S. *Nano Letters* **2009**, *9*, 4268.
- (2) Li, X.; Cai, W.; An, J.; Kim, S.; Nah, J.; Yang, D.; Piner, R.; Velamakanni, A.; Jung, I.; Tutuc, E.; Banerjee, S. K.; Colombo, L.; Ruoff, R. S. *Science* **2009**, *324*, 1312.

- (3) Hao, Y.; Bharathi, M. S.; Wang, L.; Liu, Y.; Chen, H.; Nie, S.; Wang, X.; Chou, H.; Tan, C.; Fallahazad, B.; Ramanarayan, H.; Magnuson, C. W.; Tutuc, E.; Yakobson, B. I.; McCarty, K. F.; Zhang, Y.-W.; Kim, P.; Hone, J.; Colombo, L.; Ruoff, R. S. *Science***2013**, *342*, 720.
- (4) Banszerus L., S. M., Engels, S., Dauber, J., Oellers, M., Haupt, F., Watanabe, K., Taniguchi, T., Beschoten, B., and Stampfer, C. *Science Advances***2015**, *1*, e1500222.
- (5) Dean, C. R.; Young, A. F.; Meric, I.; Lee, C.; Wang, L.; Sorgenfrei, S.; Watanabe, K.; Taniguchi, T.; Kim, P.; Shepard, K. L.; Hone, J. *Nature Nanotechnology***2010**, *5*, 722.
- (6) Jo, I.; Pettes, M. T.; Kim, J.; Watanabe, K.; Taniguchi, T.; Yao, Z.; Shi, L. *Nano Letters***2013**, *13*, 550.
- (7) Watanabe, K.; Taniguchi, T.; Niiyama, T.; Miya, K.; Taniguchi, M. *Nature Photonics***2009**, *3*, 591.
- (8) Li, X.; Magnuson, C. W.; Venugopal, A.; Tromp, R. M.; Hannon, J. B.; Vogel, E. M.; Colombo, L.; Ruoff, R. S. *Journal of the American Chemical Society***2011**, *133*, 2816.
- (9) Petrone, N.; Dean, C. R.; Meric, I.; van der Zande, A. M.; Huang, P. Y.; Wang, L.; Muller, D.; Shepard, K. L.; Hone, J. *Nano Letters***2012**, *12*, 2751.
- (10) Banszerus, L.; Schmitz, M.; Engels, S.; Goldsche, M.; Watanabe, K.; Taniguchi, T.; Beschoten, B.; Stampfer, C. *Nano Letters***2016**, *16*, 1387.
- (11) Fiori, G.; Bonaccorso, F.; Iannaccone, G.; Palacios, T.; Neumaier, D.; Seabaugh, A.; Banerjee, S. K.; Colombo, L. *Nature Nanotechnology***2014**, *9*, 768.
- (12) Shi, Y.; Hamsen, C.; Jia, X.; Kim, K. K.; Reina, A.; Hofmann, M.; Hsu, A. L.; Zhang, K.; Li, H.; Juang, Z.-Y.; Dresselhaus, M. S.; Li, L.-J.; Kong, J. *Nano Letters***2010**, *10*, 4134.
- (13) Suzuki, S.; Pallares, R. M.; Hibino, H. *Journal of Physics D-Applied Physics***2012**, *45*, 385304.
- (14) Suzuki, S.; Pallares, R. M.; Orofeo, C. M.; Hibino, H. *Journal of Vacuum Science & Technology B***2013**, *31*, 041804.
- (15) Ismach, A.; Chou, H.; Ferrer, D. A.; Wu, Y.; McDonnell, S.; Floresca, H. C.; Covacevich, A.; Pope, C.; Piner, R.; Kim, M. J.; Wallace, R. M.; Colombo, L.; Ruoff, R. S. *ACS Nano***2012**, *6*, 6378.
- (16) Sonde, S.; Dolocan, A.; Lu, N.; Corbet, C.; Kim, M. J.; Tutuc, E.; Banerjee, S. K.; Colombo, L. *2d Materials***2017**, *4*, 025052.
- (17) Kim, S. M.; Hsu, A.; Park, M. H.; Chae, S. H.; Yun, S. J.; Lee, J. S.; Cho, D. H.; Fang, W. J.; Lee, C.; Palacios, T.; Dresselhaus, M.; Kim, K. K.; Lee, Y. H.; Kong, J. *Nature Communications***2015**, *6*, 8662.
- (18) Gao, Y.; Ren, W.; Ma, T.; Liu, Z.; Zhang, Y.; Liu, W.-B.; Ma, L.-P.; Ma, X.; Cheng, H.-M. *Acs Nano***2013**, *7*, 5199.
- (19) Kim, G.; Jang, A. R.; Jeong, H. Y.; Lee, Z.; Kang, D. J.; Shin, H. S. *Nano Letters***2013**, *13*, 1834.
- (20) Song, L.; Ci, L.; Lu, H.; Sorokin, P. B.; Jin, C.; Ni, J.; Kvashnin, A. G.; Kvashnin, D. G.; Lou, J.; Yakobson, B. I.; Ajayan, P. M. *Nano Letters***2010**, *10*, 3209.
- (21) Tay, R. Y.; Griep, M. H.; Mallick, G.; Tsang, S. H.; Singh, R. S.; Tumlin, T.; Teo, E. H. T.; Karna, S. P. *Nano Letters***2014**, *14*, 839.
- (22) Kim, K. K.; Hsu, A.; Jia, X.; Kim, S. M.; Shi, Y.; Hofmann, M.; Nezich, D.; Rodriguez-Nieva, J. F.; Dresselhaus, M.; Palacios, T.; Kong, J. *Nano Letters***2012**, *12*, 161.
- (23) Muller, F.; Hufner, S.; Sachdev, H.; Gsell, S.; Schreck, M. *Physical Review B***2010**, *82*, 075405.
- (24) Behura, S.; Nguyen, P.; Che, S.; Debbarma, R.; Berry, V. *Journal of the American Chemical Society***2015**, *137*, 13060.
- (25) Kim, G.; Lim, H.; Ma, K. Y.; Jang, A. R.; Ryu, G. H.; Jung, M.; Shin, H. J.; Lee, Z.; Shin, H. S. *Nano Letters***2015**, *15*, 4769.



- (26) Gong, Y. J.; Shi, G.; Zhang, Z. H.; Zhou, W.; Jung, J.; Gao, W. L.; Ma, L. L.; Yang, Y.; Yang, S. B.; You, G.; Vajtai, R.; Xu, Q. F.; MacDonald, A. H.; Yakobson, B. I.; Lou, J.; Liu, Z.; Ajayan, P. M. *Nature Communications* **2014**, *5*, 3193.
- (27) Pakdel, A.; Zhi, C. Y.; Bando, Y.; Golberg, D. *Materials Today* **2012**, *15*, 256.
- (28) Jang, A. R.; Hong, S.; Hyun, C.; Yoon, S. I.; Kim, G.; Jeong, H. Y.; Shin, T. J.; Park, S. O.; Wong, K.; Kwak, S. K.; Park, N.; Yu, K.; Choi, E.; Mishchenko, A.; Withers, F.; Novoselov, K. S.; Lim, H.; Shin, H. S. *Nano Letters* **2016**, *16*, 3360.
- (29) Rousseas, M.; Goldstein, A. P.; Mickelson, W.; Worsley, M. A.; Woo, L.; Zettl, A. *Acs Nano* **2013**, *7*, 8540.
- (30) Wang, X. B.; Weng, Q. H.; Wang, X.; Li, X.; Zhang, J.; Liu, F.; Jiang, X. F.; Guo, H. X.; Xu, N. S.; Golberg, D.; Bando, Y. *Acs Nano* **2014**, *8*, 9081.
- (31) Yuan, M. J.; Zhou, T.; He, J.; Chen, L. F. *Applied Surface Science* **2016**, *382*, 27.
- (32) Das, M.; Basu, A. K.; Ghatak, S.; Joshi, A. G. *Journal of the European Ceramic Society* **2009**, *29*, 2129.
- (33) Bartnitskaya, T. S.; Oleinik, G. S.; Pokropivnyi, A. V.; Pokropivnyi, V. V. *Jetp Letters* **1999**, *69*, 163.
- (34) Mende, P. C.; Gao, Q.; Ismach, A.; Chou, H.; Widom, M.; Ruoff, R.; Colombo, L.; Feenstra, R. M. *Surface Science* **2017**, *659*, 31.
- (35) Park, S.; Lee, J.; Kim, H. S.; Park, J. B.; Lee, K. H.; Han, S. A.; Hwang, S.; Kim, S. W.; Shin, H. J. *Acs Nano* **2015**, *9*, 633.
- (36) Kong, X. H.; Ji, H. X.; Piner, R. D.; Li, H. F.; Magnuson, C. W.; Tan, C.; Ismach, A.; Chou, H.; Ruoff, R. S. *Applied Physics Letters* **2013**, *103*, 043119.
- (37) Gao, Q.; Mende, P. C.; Widom, M.; Feenstra, R. M. *Journal of Vacuum Science & Technology B* **2015**, *33*, 02B105.
- (38) Feenstra, R. M.; Srivastava, N.; Gao, Q.; Widom, M.; Diaconescu, B.; Ohta, T.; Kellogg, G. L.; Robinson, J. T.; Vlassiuk, I. V. *Physical Review B* **2013**, *87*, 041406(R).
- (39) Srivastava, N.; Gao, Q.; Widom, M.; Feenstra, R. M.; Nie, S.; McCarty, K. F.; Vlassiuk, I. V. *Physical Review B* **2013**, *87*, 245414.
- (40) Orofeo, C. M.; Suzuki, S.; Kageshima, H.; Hibino, H. *Nano Research* **2013**, *6*, 335.
- (41) Luxmi; Srivastava, N.; Feenstra, R. M.; Fisher, P. J. *Journal of Vacuum Science & Technology B* **2010**, *28*, C5C1.
- (42) Frueh, S.; Kellett, R.; Mallery, C.; Molter, T.; Willis, W. S.; Kinglond, C.; Suib, S. L. *Inorganic Chemistry* **2011**, *50*, 783.
- (43) Jung, C. H.; Lee, M. J.; Kim, C. J. *Materials Letters* **2004**, *58*, 609.
- (44) Hubacek, M.; Ueki, M. *Journal of Solid State Chemistry* **1996**, *123*, 215.
- (45) Moddeman, W. E.; Burke, A. R.; Bowling, W. C.; Foote, D. S. *Surface and Interface Analysis* **1989**, *14*, 224.
- (46) National Institute of Standards and Technology:  
<https://srdata.nist.gov/xps/ElmComposition.aspx>.
- (47) Na, S. R.; Rahimi, S.; Tao, L.; Chou, H.; Ameri, S. K.; Akinwande, D.; Liechti, K. M. *Nanoscale* **2016**, *8*, 7523.
- (48) Chou, H.; Ismach, A.; Ghosh, R.; Ruoff, R. S.; Dolocan, A. *Nature Communications* **2015**, *6*, 7482.
- (49) Elko-Hansen, T. D. M.; Dolocan, A.; Ekerdt, J. G. *Journal of Physical Chemistry Letters* **2014**, *5*, 1091.
- (50) Yang, X. X.; Guan, Z. X.; Zeng, M.; Wei, J. K.; Wang, W. L.; Bai, X. D. *Small* **2013**, *9*, 1353.
- (51) Wallace, R. M. *ECS Transactions* **2014**, *64*, 109.
- (52) Addou, R.; Colombo, L.; Wallace, R. M. *Acs Applied Materials & Interfaces* **2015**, *7*, 11921.

1  
2  
3  
4  
5  
6  
7  
8  
9  
10  
11  
12  
13  
14  
15  
16  
17  
18  
19  
20  
21  
22  
23  
24  
25  
26  
27  
28  
29  
30  
31  
32  
33  
34  
35  
36  
37  
38  
39  
40  
41  
42  
43  
44  
45  
46  
47  
48  
49  
50  
51  
52  
53  
54  
55  
56  
57  
58  
59  
60

---